JACS
JOURNAL OF THE AMERICAN CHEMICAL SOCIETY

Article

pubs.acs.org/JACS

# Lithiation Thermodynamics and Kinetics of the $TiO_2$ (B) Nanoparticles

Xiao Hua,[*,†,‡] Zheng Liu,[§,∥] Michael G. Fischer,[†] Olaf Borkiewicz,[⊥] Peter J. Chupas,[⊥] Karena W. Chapman,[⊥] Ullrich Steiner,[†] Peter G. Bruce,[#] and Clare P. Grey[*,‡]

[†]Adolphe Merkle Institute, University of Fribourg, Chemin des Verdiers 4, 1700 Fribourg, Switzerland
[‡]Department of Chemistry, University of Cambridge, Lensfield Road, Cambridge, CB2 1EW, United Kingdom
[§]School of Applied Physics and Materials, Wuyi University, Jiangmen, Guangdong 529020, China
[∥]School of Chemistry, University of St. Andrews, North Haugh, St. Andrews, Fife, KY16 9ST, United Kingdom
[⊥]X-ray Science Division, Advanced Photon Source, Argonne National Laboratory, Argonne, Illinois 60439, United States
[#]Departments of Materials and Chemistry, University of Oxford, Parks Road, Oxford, OX1 3PH, United Kingdom

Supporting Information

**ABSTRACT:** $TiO_2$ (B) has attracted considerable attention in recent years because it exhibits the largest capacity among all studied titania polymorphs, with high rate performance for Li intercalation being achieved when this material is nanostructured. However, due to the complex nature of its lithiation mechanism and practical challenges in probing Li structure in nanostructured materials, a definitive understanding of the lithiation thermodynamics has yet to be established. A comprehensive mechanistic investigation of the $TiO_2$ (B) nanoparticles is therefore presented using a combination of *in situ*/*operando* X-ray pair distribution function (PDF) and electrochemical techniques. The discharge begins with surface reactions in parallel with Li insertion into the subsurface of the nanoparticles. The Li bulk insertion starts with a single-phase reaction into the A2 site, a position adjacent to the *b*-channel. A change of the Li diffusion pathway from that along this open channel to that along the *c*-direction is likely to occur at the composition of $Li_{0.25}TiO_2$ until $Li_{0.5}TiO_2$ is attained, leading to a two-step A2-site incorporation with one step kinetically distinct from the other. Subsequent Li insertion involves the C′ site, a position situated inside the channel, and follows a rapid two-phase reaction to form $Li_{0.75}TiO_2$. Due to the high diffusion barrier associated with the further lithiation, Li insertion into the A1 site, another position adjacent to the channel neighboring the A2 sites, is kinetically restricted. This study not only explores the lithiation reaction thermodynamics and mechanisms of nanoparticulate $TiO_2$ (B) but also serves as a strong reference for future studies of the bulk phase, and for future calculations to study the Li transport properties of $TiO_2$ (B).

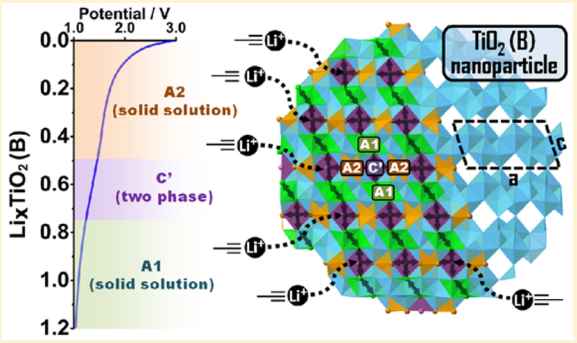


## INTRODUCTION

$TiO_2$ polymorphs have attracted significant attention in the field of photocatalysis and solar energy conversion due to their high stability, low cost and efficient photoactivity.[1,2] Their ability to accommodate Li also makes $TiO_2$ an attractive anode candidate for lithium-ion batteries (LIBs). Among the common polymorphs, anatase is the most studied phase due to its higher practical capacity in comparison to those of rutile and brookite. Recently, there has been a growing interest in the bronze (B) phase, which is a promising alternative to anatase. The unique structure of $TiO_2$ (B) can, in principle, accommodate a theoretical maximum of 1.25 Li per formula unit,[3] larger than the 1 Li per formula unit for anatase. The presence of open channels along the *b*-axis, in association with Li diffusion pathways with low activation energy, is believed to be the reason for its excellent rate capability and has led to a growing interest in the study of its "pseudocapacitive" properties.[4] We note that the term "pseudocapacitive" or "capacitive" is used by some researchers even in intercalation systems, when diffusion of the intercalating ions is not rate limiting.[5] Synthetic efforts have yielded $TiO_2$ (B) with various morphologies that deliver enhanced electrochemical performance relative to the bulk form. However, a fundamental understanding of the lithiation thermodynamics and kinetics of this material has yet to be achieved.

The $TiO_2$ (B) has a monoclinic structure ($C2/m$) which contains two different Ti positions and four distinct O sites. Based on their coordination to Ti atoms and using the labeling introduced by Arrouvel et al.,[6] the O atoms (shown in Figure 1a) can be grouped as $O_{br}$ (bridging oxygens that connect the double $TiO_6$-octahedral layers[7]), $O_{4f}$ (4-fold coordination), and $O_{3f}$ (two symmetry-inequivalent O atoms that are both 3-fold coordinated). Three Li sites have been identified by earlier

**Received:** May 20, 2017
**Published:** August 5, 2017

  

DOI: 10.1021/jacs.7b05228
J. Am. Chem. Soc. 2017, 139, 13330−13341

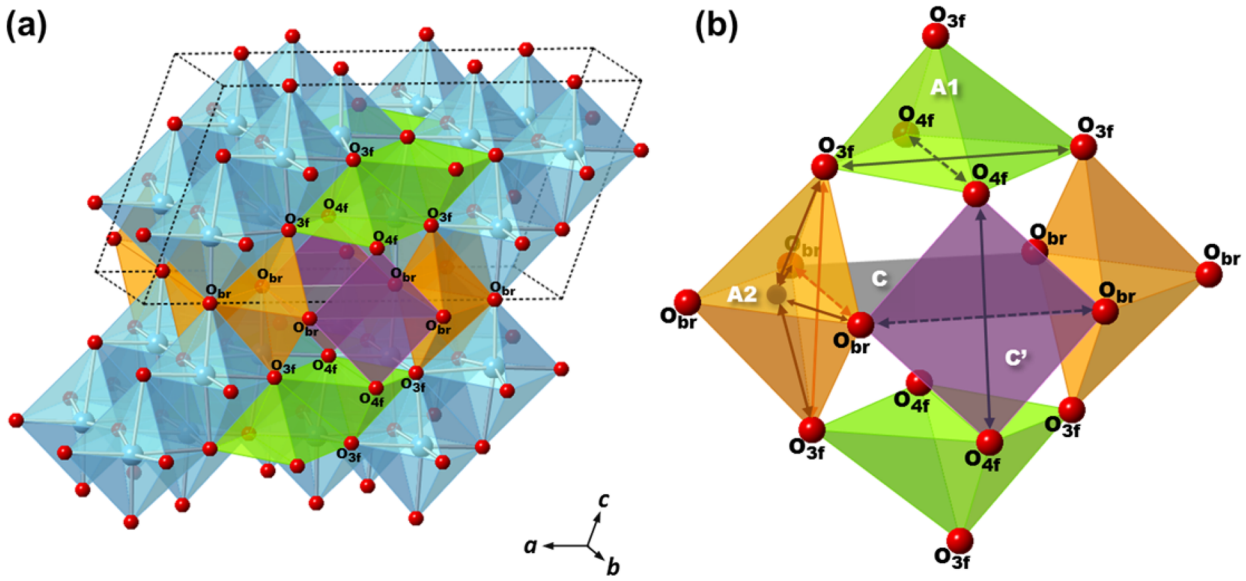


**Figure 1.** (a) Crystal structure of $TiO_2$ (B) containing a $TiO_6$-octahedral framework (Ti: blue; O: red) and the Li sites, A1, A2, C, and C′, highlighted using green, orange, gray, and purple colors, respectively; the unit cell is illustrated using black dashed lines, and three types of oxygen atoms are labeled accordingly. The Li sites coordinated with these labeled oxygens are shown in (b), where (dashed) arrows indicate distances between either the two O atoms, $d(O-O)_{diagonal}$, or the Li and O atoms in the A2 site, $d(Li-O)$.

computational studies[6,8] and were labeled as A1, A2, and C.[6] The Li atoms in A1 and A2 sites both adopt a distorted square-pyramidal geometry (5-fold coordination), while the ideal C site at (0.0, 0.5, 0.0) has a square-planar environment for Li.[6,8] In practice, the C site is too large for Li and some theoretical studies located the Li in this C site but slightly off-centered[6,8] along the *b*-direction plane in a new position with coordinates (0.0, 0.6, 0.0)[3] (2-fold coordinated to the nearest $O_{br}$). Theoretical studies later performed by Koudriachova[9] and Dalton et al.[3] both proposed a new Li position (0.0, 0.0, 0.0) which was labeled as the C′ site and has lower energy than the C site at higher Li concentrations. This C′ site also has a square-planar geometry and is corner-shared with the neighboring pyramidal A sites.

Most studies[6,8,10,11] suggested similar binding energies for site C and A2 in the dilute limit with an energy difference between these two sites that is much smaller than that between A1 and C or A2 sites. Furthermore, the energetic trends in $TiO_2$ (B) were found to be very sensitive to the choice of functional in the density functional theory (DFT) calculation.[10] Given the uncertainty in the calculations (where the various computational investigations are summarized in the Supporting Information (SI)), it is hard to predict the extent of A2 and C site occupation (particularly at low Li concentrations) and additional experimental evidence is required. To this end, numerous experimental approaches have been applied utilizing several *ex situ* and *in situ*/*operando* characterization tools[12−15] including X-ray absorption spectroscopy (XAS) and neutron or X-ray diffraction (ND or XRD). Unfortunately, as in the theoretical studies there is again a lack of consistency between these reported experimental analyses (also summarized in the SI): the long-range structural studies using ND[13] and XRD[15] giving conflicting results.

As an alternative approach, $^6$Li NMR spectroscopy[16] was applied to study the Li structure of the lithiated $TiO_2$ (B). The obtained spectra showed multiple resonances confirming the presence of multiple Li sites. However, those peaks overlapped significantly and were dominated by one resonance attributed to the surface Li, thus making the peak deconvolution and site assignment difficult. A complementary method to probe the local structure is the pair distribution function (PDF) obtained from the X-ray total scattering experiment. Due to the low X-ray scattering power of Li atoms, it is challenging to determine the Li positions in a crystal structure directly from the X-ray data, especially for the samples with low Li concentrations. The PDF method, however, enables an accurate investigation of the local structure for the Ti and O atoms, which can be used indirectly to study the geometry of Li sites. A continuous collection of high quality *in situ* PDF patterns further makes it possible to examine the geometric evolution of those Li positions, in principle allowing for a reliable interpretation of the reaction mechanism.

In this Article, we present a comprehensive mechanistic investigation of $TiO_2$ (B) nanoparticles using *in situ*/*operando* (hereinafter referred to as only *in situ*) PDF technique. We demonstrate that the Li occupancies and local environments, although difficult to probe using routine analytical methods, can be accessed indirectly via a careful examination of the X-ray total scattering data. The investigation helps unravel the reaction mechanism and test the various thermodynamic models proposed based on numerous theoretical and experimental reports. In addition, a series of electrochemistry experiments were conducted and Li mobility, charge storage behavior, and temperature effects were evaluated. This allows us to study the kinetic properties of the material and to deduce plausible Li transport pathways based on our proposed lithiation mechanism. Oblate-shaped[7] $TiO_2$ (B) nanoparticles were chosen as our model compound because they exhibit the best capacity and rate performance among all the reported morphologies.[17] Due to possible particle-size and/or morphology dependent charge storage behavior,[11,18] which could be one of the origins of the inconsistent results in the literature, the conclusions drawn from the nanoparticles may deviate from those obtained from the bulk phase. However, considering the poor understanding of the reaction mechanism for $TiO_2$ (B), our results will serve as a fundamental basis with which to


DOI: 10.1021/jacs.7b05228
J. Am. Chem. Soc. 2017, 139, 13330−13341

explore the effect of size and shape on the lithiation thermodynamics. In addition, the Li transport properties determined in this study for the nanoparticles, i.e., a Li migration pathway dominated by the *c*-axis instead of *b*-channel diffusion, could offer plausible explanations for the morphology-dependent kinetic behavior seen in various nanostructured phases, providing a guideline for future material design.

## EXPERIMENTAL SECTION

**Materials Preparation and Electrochemistry Measurements.** The synthesis of the $TiO_2$ (B) nanoparticles (via hydrothermal methods) followed the same method as reported previously.[7,17] The electrodes were prepared by mixing the active material ($TiO_2$ (B) nanoparticles), Kynar 2801 (polyvinylidenefluoride (PVDF)), and Super P carbon (TIMCAL C65) in a weight ratio of 70:20:10 in *N*-methylpyrrolidone (NMP). The slurry was cast onto an aluminum foil using the doctor-blade method. After solvent evaporation at room temperature and heating at 80 °C under vacuum overnight, the electrode sheet was cut into discs (with 1.27 cm in diameter and an average total mass loading of about 2.0 mg) before being transferred into an Ar-filled glovebox (MBraun). Swagelok cells were assembled with a Celgard separator, a Li metal foil as the counter electrode, and l M $LiPF_6$ in ethylene carbonate (EC)/dimethyl carbonate (DMC) solution (volume ratio 1:1) as the electrolyte (Solvionic). The materials with specific Li content for *ex situ* experiments were collected from batteries that were stopped at the desired capacity or potential. Prior to the measurement, the powder was rinsed using DMC and dried in an Ar-filled glovebox.

Galvanostatic measurements were performed at either room temperature (rt) 25 or 50 °C within the potential window of 2.5−1.0 V (vs Li metal, the same as follows) using a current rate of *C*/20 (unless stated otherwise) where *C* refers to theoretical specific capacity (335 mAh/g)[17] and 20 corresponds to 20 h to reach the theoretical capacity. Galvanostatic intermittent titration (GITT) experiments were performed at 50 °C under a *C*/20 rate with a 0.75-h current step and a 4-h relaxation period from open circuit voltage to 1.0 V. Diffusion coefficients $D_{Li}$ were extracted from the GITT data using Fick's law:[19] $D_{Li} = \frac{4}{\pi}\left(\frac{IV_M}{Z_A FS}\right)^2\left(\frac{dE_x/dx}{dE_t/dt^{1/2}}\right)^2$, $(t \ll L^2/D_{Li})$ under a provisional assumption that the lithiation follows a single-phase reaction (see later discussion). *L* (cm) is the characteristic diffusion length; *F* (96 485 C/mol) is the Faraday constant; $V_M$ (21.83 $cm^3$/mol) is the molar volume of the electrode material. A constant $V_M$ was applied as the volume increase upon lithiation leads to negligible changes in the magnitude of the $D_{Li}$; *I* ($1.14 \times 10^{-4}$ A) is the applied pulse current; *S* (1.27 $cm^2$) is the contact area between the electrode and electrolyte. In this study, the apparent surface area of the electrode was used as an approximation; thus, overestimation of the derived $D_{Li}$ is expected. Term $dE_x/dx$ represents the slope of coulometric titration curve which is obtained by plotting the equilibrium potential versus the Li content; the term $dE_t/dt^{1/2}$ corresponds to the slope of the straight line in the potential curve of each current pulse (*E* vs $t^{1/2}$).

Cyclic voltammetry (CV) measurements were performed at both rt (25 °C) and 50 °C in the same potential window of 2.5−1.0 V with sweep rates of 0.5, 1.0, 2.0, 3.0, 4.0, and 5.0 mV/s. The 50 °C experiment started with an additional 5.0 mV/s scan to promote the irreversible electrolyte decomposition (see later discussion). Charge storage behavior was evaluated based on the assumption that the current responses at a fixed potential can be represented by a combination of nominally surface (capacitive) effects ($k_1$) and a diffusion-controlled (insertion) process ($k_2$) which follows equation: $I(V) = k_1 v + k_2 v^{1/2}$, where *I* is the current and *v* (mV/s) corresponds to the sweep rate of the CV measurement.[5] Quantification of $k_1$ and $k_2$ was performed by a linear fitting of $I/v^{1/2}$ at different potentials against $v^{1/2}$.

**PDF via X-ray Total Scattering.** The X-ray total scattering data were collected both *ex situ* and *in situ* at beamline 11-ID-B at the Advanced Photon Source (APS) at Argonne National Laboratory using an amorphous Si two-dimensional (2D) detector with an X-ray energy of 58 keV ($\lambda$ = 0.2127 Å). All experiments were conducted in transmission geometry. *Ex situ* measurements were performed on powdered samples that were sealed in a Kapton capillary (Ø 1.0 mm) under an Ar atmosphere. For the *in situ* experiment, electrode pellets that contained 60 wt % of $TiO_2$ (B) nanoparticles, 20 wt % of Super P carbon ,and 20 wt % of PTFE were prepared and assembled into the AMPIX cell[20] with a glass fiber as a separator, a Li metal foil as the counter electrode, and l M $LiPF_6$ in EC/DMC (volume ratio 3:7) solution (Tomiyama Pure Chemical Industries) as the electrolyte.[21] The *in situ* galvanostatic measurement was performed at 50 °C using a *C*/20 rate. Additional measurements including a sample of Super P carbon and an empty Kapton capillary, as well as a reference AMPIX cell containing all the components in the same mass ratio except the active material, were performed under the same experimental conditions to obtain the background. Intensity data versus *Q* were obtained by converting the integrated 2D image-plate data using the Fit2D software.[22] Data corrections including background subtraction, sample self-absorption, multiple scattering, X-ray polarization, and Compton scattering were employed to obtain the normalized scattering intensity *S*(*Q*) using the PDFgetX2 program.[23] Specifically, $Q_{max}$ of 25.0 and 18.0 $Å^{-1}$ were used for the PDF extraction of the *ex situ* and *in situ* data, respectively. The reduction of the $Q_{max}$ for the *in situ* measurement was due to the limitation of the maximum accessible scattering angle by the scattering aperture in the AMPIX cell.[24] Real-space least-squares refinement was performed using the PDFgui[25] program. Previously collected scattering data for the Ni standard were processed and refined to obtain the instrumental damping factor. Structure modeling and diffraction data simulation were performed using the method reported previously[7] with the DISCUS program.[26]

## RESULTS

**Electrochemistry.** The galvanostatic measurement performed at room temperature (Figure 2a) shows that the capacity of the material reaches about 1 Li per formula unit within a voltage window of 3.0−1.0 V in the first discharge. A 25% capacity loss in the first cycle was observed with a capacity retention of 70% after 10 cycles (Figure S1a). This reversible capacity corresponds to 0.70−0.75 Li per formula unit (within the voltage window of 3.0−1.0 V).

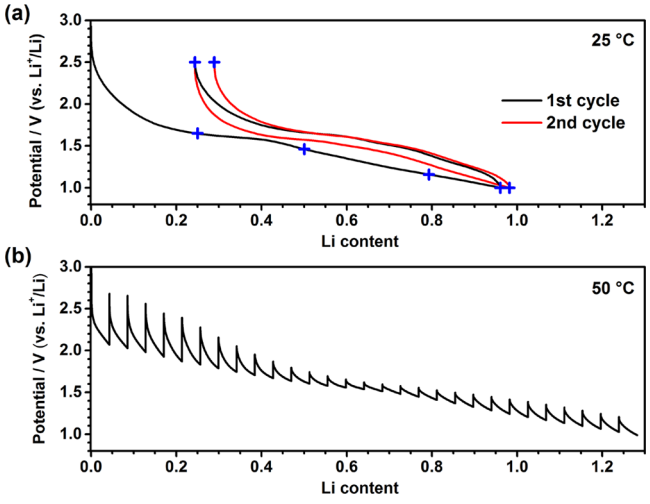


**Figure 2.** (a) Potential curve including the first (black) and second (red) cycles from the galvanostatic measurement performed at room temperature. Blue crosses mark the states where *ex situ* PDF patterns were collected. (b) Potential curve of the GITT measurement performed at 50 °C.


DOI: 10.1021/jacs.7b05228
J. Am. Chem. Soc. 2017, 139, 13330−13341

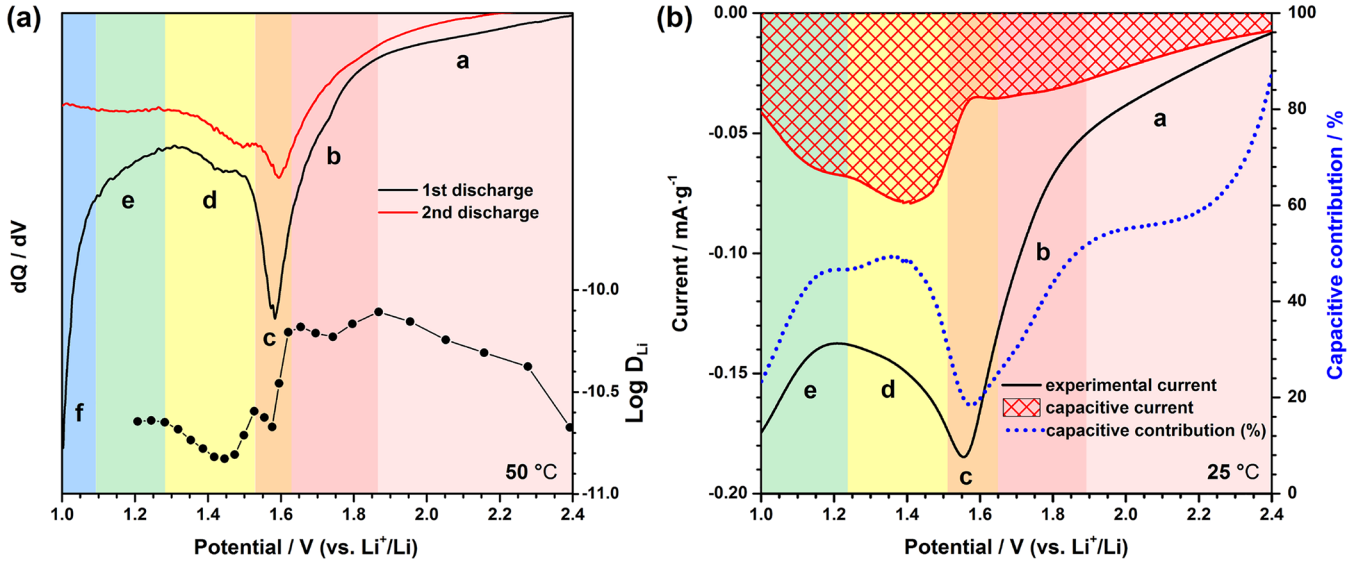


**Figure 3.** (a) d$Q$/d$V$ plot of the first two discharge steps from the galvanostatic measurement (shown in Figure S1b) in comparison with the $D_{Li}$ plotted against the equilibrium potential of each titration step from the GITT measurement performed at 50 °C. (b) Current response (black solid) of the discharge scan from the CV collected at 25 °C with a sweep rate of 0.5 mV/s in comparison with its capacitive component (red grid) derived from the analysis of the charge storage behavior. The percentage of this "capacitive" contribution (blue dotted line) is also included, "capacitive" indicating a process whose rate limiting step does not appear to correspond to the diffusion of Li in the bulk, according to ref 5. In both figures, distinct reaction processes are labeled accordingly and highlighted using a color code consistent with all the following figures.

The GITT data (Figure 2b) collected at 50 °C show an increase in capacity to about 1.3 Li per formula unit, in agreement with the capacity of the first discharge from the galvanostatic cycling performed at the same temperature (Figure S1b). The elevated temperature, however, showed little influence on the subsequent discharge and charging processes where the accessible capacity remains 0.6−0.7 Li (Figure S1b). This suggests that the additional capacity beyond 1 Li is due to irreversible side reactions, an even larger irreversible capacity loss being observed as compared to the room-temperature measurement. A closer examination of the GITT profile shows that the relaxation periods are associated with a voltage increase of various magnitudes to reach equilibrium at different states of discharge, reflecting multiple kinetically different steps. These steps are more evident in Figure 3a, where the extracted $D_{Li}$ from the GITT data shows an evolution that matches well with the features in the d$Q$/d$V$ curve from the galvanostatic cycling. We have divided the plot into six regions (labeled as "a"−"f") with each associated with distinct discharge kinetics. Judging by a visual comparison between the discharge and charge profile (Figure S2a and S2e), all of these steps seem at least partly reversible apart from the process "f". Process "f" takes place below 1.1 V on discharge at high temperature and is only apparent in the first discharge, suggesting that it is related to electrolyte decomposition forming an inert solid-electrolyte interface (SEI) layer that prevents further degradation of the electrolyte in subsequent discharge cycles. Its absence at room temperature (Figures 3b and S2b) indicates this parasitic reaction is temperature sensitive and is promoted by an increased operating temperature.

To supplement the information concerning the kinetic properties acquired from the GITT analysis (50 °C) and also to relate the high temperature behavior to the rt performance, we also examined the CV data at both temperatures (Figure S2c−d). Based on a visual comparison of the (normalized) CV scans performed at the same rate but at different temperatures (Figure S2e), it is seen that an increased temperature is associated with a higher magnitude of current (leading to more pronounced redox features) and a decrease in the splitting between the anodic and cathodic peaks within each redox couple. These observations are consistent with the results previously reported for anatase indicating a temperature dependence of the CV current and kinetically hindered redox reactions.[27] Further study of these CV data follows the same protocol and analysis reported previously on the anatase $TiO_2$ nanoparticles by Wang et al.[5] In this approach, the current $I(V)$ is formally separated into a faster process (the so-called capacitive process, $k_1$) and a slower process (nominally the diffusion-controlled intercalation process, $k_2$) following the equation: $I(V) = k_1v + k_2v^{1/2}$, $v$ (mV/s) being the sweep rate of the CV measurement. This analysis was performed on the discharge sweep for both the 25 °C (Figure 3b) and 50 °C (Figure S2f) data. The results between these temperatures share the same kinetically different steps as those processes derived from the GITT analysis (Figure 3a), implying identical redox processes regardless of the temperature. Taking the rt case as an example (Figure 3b), the lithiation of $TiO_2$ (B) nanoparticles starts with a rapid process "a", where the Li insertion process is not diffusion-limited; it is followed by an increasing contribution from a diffusion-controlled current in process "b", suggesting charge transfer via Li insertion in the bulk. The first rapid process, although termed a "(pseudo)-capacitive" process within the analysis of Wang et al.,[5] may simply be viewed as a process that is not limited by bulk diffusion; it can still involve a Faradaic process. This "diffusion" current reaches a maximum in process "c" but becomes less prominent in the following step "d" where a significant increase in a capacitive contribution is observed, suggesting an insertion process that is more rapid than "c". The reaction terminates with step "e" with an increased diffusive current contribution corresponding to a Faradaic process similar to "b" and "c". Comparing the charge storage kinetics of each insertion step between the 25 and 50 °C results, the most prominent effect of


DOI: 10.1021/jacs.7b05228
J. Am. Chem. Soc. 2017, 139, 13330−13341

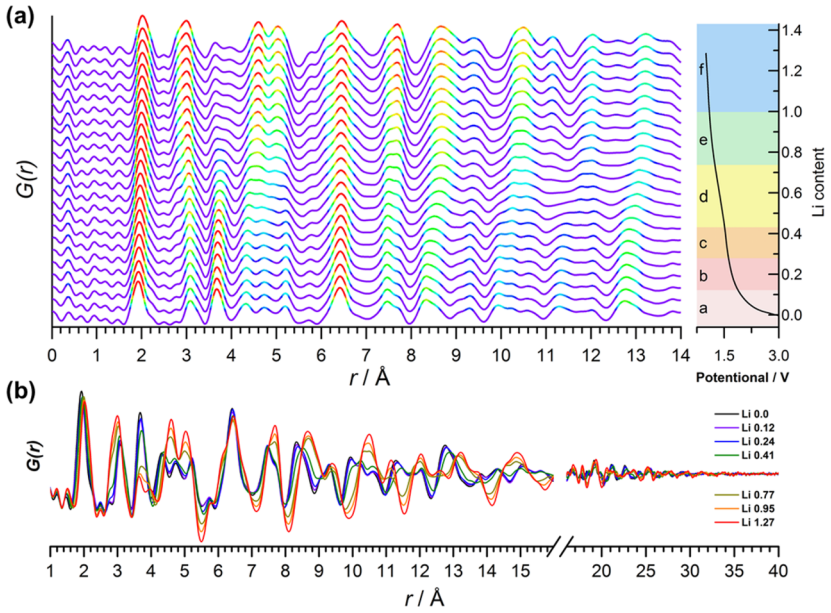


**Figure 4.** (a) *In situ* PDF patterns collected from the first discharge of the galvanostatic measurement (*C*/20, 50 °C) with the corresponding potential curve (with distinct processes labeled and highlighted in the same way as those in Figure 3), shown on the right, indicating the Li content of each PDF pattern. The colors in the PDF pattern reflect relative peak intensities. (b) Selected *in situ* PDFs are overlaid to allow a clearer comparison (note the different scales of the *x*-axes).

the increasing temperature is reflected by an increase of a "diffusive" contribution to the processes "a" and "d" (which are largely "capacitive" processes at 25 °C), while the processes "b", "c", and "e" show little change. This observation shows that the temperature dependence of these "capacitive" processes differs considerably from that of the diffusion-controlled redox processes, implying the nature of steps "a" and "d" are fundamentally different from those of "b", "c", and "e".

**PDF.** The plot containing the series of *in situ* PDF patterns is shown in Figure 4. The PDFs at low lithiation levels, Li 0.12 and Li 0.24, show nearly identical profiles as the pristine (Li 0.0) pattern with only subtle changes in peak intensities, suggesting the reactions responsible for processes "a" and "b" do not involve a discernible structural evolution and must be dominated by surface processes. Gradual changes in peak intensities associated with small peak shifts are evident in the patterns from Li 0.24 to Li 0.41 (process "c") and from Li 0.77 to Li 1.27 (process "e" and "f"), whereas a significant transformation occurs in process "d" between Li 0.41 and Li 0.77. These observations imply that a structural change proceeds from Li 0.24 all the way to the end of discharge at Li 1.27 (corresponding to 1.0 V under 50 °C); a drastic structural evolution takes place in process "d" involving a phase transformation that is significantly different from the others.

A comparison of the *ex situ* PDF patterns obtained at the end of the first two cycles (i.e., at the top of charge) with that obtained in the first discharge at the same Li content ($Li_{0.25}TiO_2$) shows almost identical patterns (Figure S3a). This indicates a reversible lithiation, the "fully" delithiated state retaining a local structure closer to that of $Li_{0.25}TiO_2$. The *ex situ* PDFs for the end of the first two discharge cycles at Li 1.0 also show identical patterns (Figure S3b) but with broader peak widths and lower peak intensities as compared to the *in situ* pattern of the equivalent state (Li 1.0). These discrepancies reflect a structural change due to relaxation and can be ascribed to a lithiation-induced strain-driven disorder which was previously investigated and modeled.[7]

A structure refinement against the whole series of the *in situ* PDFs was performed in the *r*-range 1.5−25 Å using the pristine $TiO_2$ (B) structure ($C2/m$)[28] with Li atoms excluded due to their low X-ray scattering power. The agreement factor $R_w$[29] from each refinement and the obtained crystallographic parameters are shown in Figure 5. The evolving trend of these parameters can be divided into several regions consistent with the reaction processes (a−f). Interestingly, a significant increase of 6% in the unit cell volume coincides with a significant change of atomic displacement parameter (ADP) U in region "d". In addition, these changes are associated with very large $R_w$ values with the maximum located in the center of the region "d" (Li 0.59). These observations, in agreement with the aforementioned large profile change of the PDF patterns in the same region, imply that the corresponding reaction "d" is fundamentally different from the others and likely involves a two-phase reaction. This two-phase reaction reaches 50% molar percentage for each component at Li 0.59 (about the center of region "d"), leading to the poorest agreement in the single-phase refinement (hence the largest $R_w$). Thus, a two-phase refinement was attempted for the PDFs in region "d" against the two structures acquired from the single-phase refinement for the states of Li 0.41 and Li 0.77. Apart from phase ratios between the two structures, all the other variables were constrained and not refined. The results show reduced $R_w$ values with the most significant improvement observed for the state of Li 0.59 from $R_w$ = 0.27 to 0.20 (see Figure S4a−b for the comparison between the two refinements and the respective PDF contributions from the two phases); moreover, the PDFs in this region "d" can be fitted by using a linear combination of the patterns from the Li 0.41 and Li 0.77 compositions (Figure S4c), consistent with the two-phase mechanism where the linear increase in the fraction of one phase is accompanied by the linear decrease of the other. To investigate whether phase coexistence within one particle occurs during the phase transition, a two-phase refinement was attempted again without constraining the particle sizes (average


DOI: 10.1021/jacs.7b05228
J. Am. Chem. Soc. 2017, 139, 13330−13341

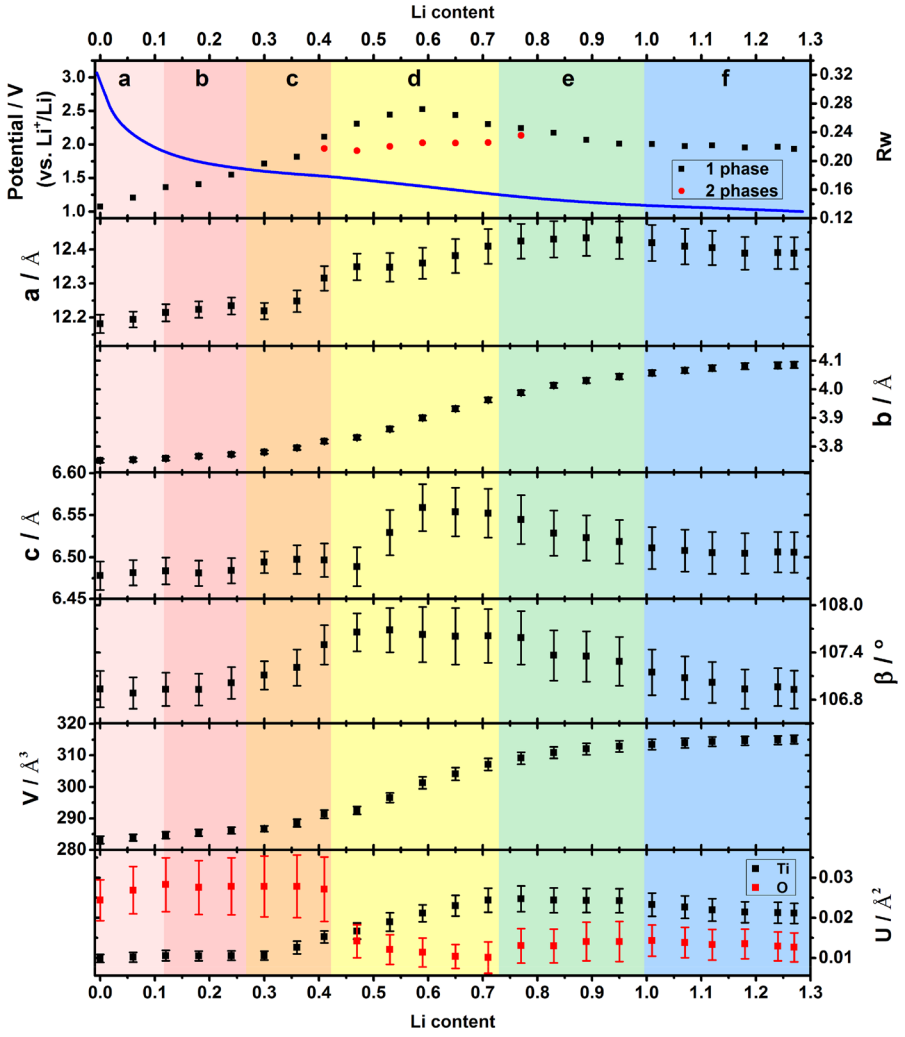


**Figure 5.** Evolution of the parameters derived from the PDF refinement as a function of the Li content, containing the agreement factor ($R_w$) for single-phase (black square) and two-phase (red circle) refinements, lattice constants ($a$, $b$, $c$ and $\beta$), unit cell volume, and atomic displacement parameters (U) for Ti (black) and O (red). These results are compared with the corresponding potential curve (blue line) obtained from the *in situ* galvanostatic measurement with distinct processes labeled and highlighted accordingly.

coherent length of the particles from each phase). The results reveal no change in particle sizes for both phases throughout reaction "d", indicating that few (if any) particles contain both phases *within the same particle*. This suggests that the two-phase reaction takes place via a particle-by-particle transformation, the second phase, once it has formed reacting quickly to completion within the individual nanoparticle, as has been observed for other nanoparticle systems.[18,30,31]

## DISCUSSION

**Lithiation Thermodynamics.** *A. Li Site Occupation.* The combination of the electrochemical and PDF analyses suggested a multiple-step lithiation for the $TiO_2$ (B) nanoparticles. To test the validity of the various proposed lithiation mechanisms, the most intuitive strategy is to obtain structural information associated with Li occupancies directly. However, the low X-ray scattering power of Li makes it challenging to acquire crystallographic information on Li from the X-ray scattering data straightforwardly, especially for the samples with low Li content. An alternative approach based on the current scattering data is to deduce the occupation of Li sites indirectly by evaluating the geometries of all Li site candidates through a careful analysis of the Ti and O local structures. The four interstitial sites (A1, A2, C, and C′) surrounding or within the *b*-channel are highlighted in Figure 1b. The diagonals of the square-planar site C′ and of the bases of the 5-coordinated square-pyramidal A sites are all marked. Thus, sites A1 and A2 are defined by a volume, while site C′ is described by the area of the square formed by two $O_{4f}$ and two $O_{br}$ oxygen atoms (Figure 1b). According to the Shannon crystal ionic radii,[32] $O^{2-}$ has a radius of 1.21 to 1.26 Å corresponding to II to IV coordination, respectively, and the $Li^+$ ion has a radius of 0.73 and 0.90 Å for IV and VI coordination, respectively. These radii values allow us to approximate a length of 1.94 (= 1.21 + 0.73) Å for the minimum and 2.16 (= 1.26 + 0.90) Å for the maximum distances between Li and O atoms (denoted as $d(\mathrm{Li-O})_{min}$ and $d(\mathrm{Li-O})_{max}$ respectively) to form stable O-coordinated Li environments in a solid. Li−O distances within this range in various coordinated environments have been reported in many titanates: 1.96 Å (average) from a distorted square-planar geometry in $Li_2Ti_6O_{13}$ ($C2/m$),[33] 2.01 Å for tetrahedra in $Li_4Ti_5O_{12}$ ($Fd\bar{3}m$),[34] 1.97−2.05 Å for 5-fold coordination in $Li_{0.5}TiO_2$ (*Imma*, also known as the orthorhombic lithiated-anatase),[35] and 2.04−2.13 Å for 6-fold


DOI: 10.1021/jacs.7b05228
J. Am. Chem. Soc. 2017, 139, 13330−13341

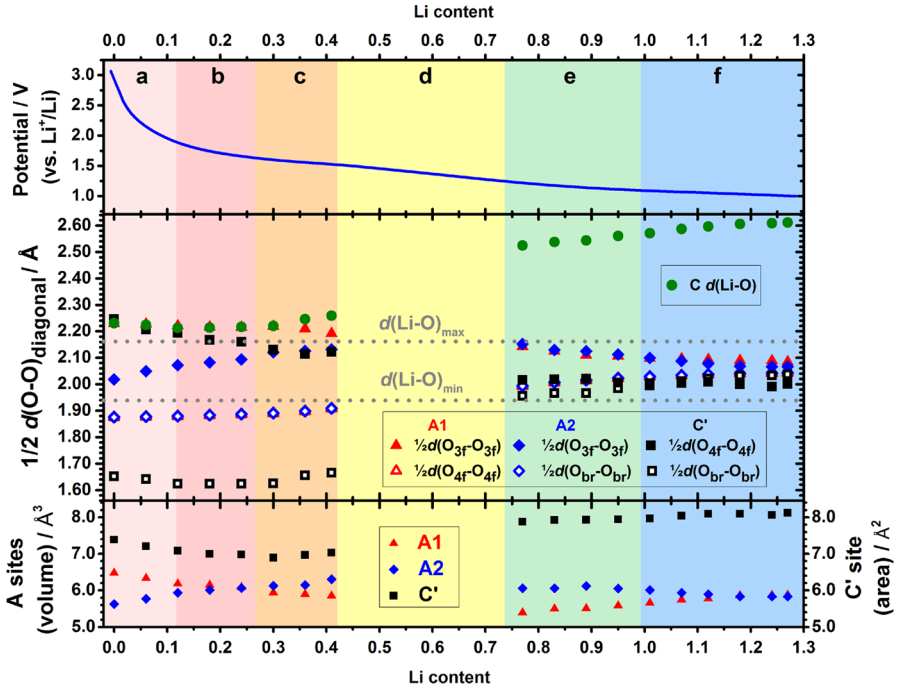


**Figure 6.** Evolution of the 1/2 $d(O-O)_{diagonal}$ and geometric size as a function of Li content for sites A1 (red triangle), A2 (blue rhombus), and C′ (black square) evaluated from the structure refined in the single-phase PDF refinement. The A and C′ sites are defined by their volume and area, respectively. The $d(Li-O)$ in site C (green circle) is additionally included in the distance comparison. The *in situ* potential curve (blue line) is also shown on top with distinct processes labeled and highlighted accordingly.

coordination in $Li_2TiO_3$ ($C2/c$).[36] In the bronze phase, for the A sites to accommodate Li, half the distance between the diagonal O atoms, denoted as 1/2 $d(O-O)_{diagonal}$, must be no more than $d(Li-O)_{max}$; for site C′ to host Li, sitting on the plane, the relationship $d(Li-O)_{min} \leq 1/2\, d(O-O)_{diagonal} \leq d(Li-O)_{max}$ needs to be valid. (A larger Li−O distance could be accommodated by $Li^+$ moving off the plane.) This is illustrated in Figure 1b for site A2 where both relationships $d(Li-O)_{max} \geq 1/2\, d(O_{3f}-O_{3f})$ and $d(Li-O)_{max} \geq 1/2\, d(O_{br}-O_{br})$ need to be fulfilled to accommodate Li.

With these criteria in mind, the Li site occupation was studied indirectly by tracking these geometric changes as a function of Li concentration. To this end, evolutions of the 1/2 $d(O-O)_{diagonal}$ and the geometric sizes of the corresponding sites as a function of Li content are shown in Figure 6, where the $d(Li-O)$ in the C site with Li coordinates (0.0, 0.6, 0.0) is also included. These values were obtained from the structures generated by the aforementioned PDF single-phase refinement. Despite numerous processes revealed by the electrochemical studies (Figure 3a), the changes of the site geometries reflect only a few different mechanisms for lithiation. The participation of the C site can be ruled out at all Li contents, as $d(Li-O)$ is always larger than $d(Li-O)_{max}$. For sites A1, A2, and C′, 1/2 $d(O_{3f}-O_{3f})$ in A1 is larger than $d(Li-O)_{max}$ and the 1/2 $d(O_{br}-O_{br})$ in C′ is much smaller than $d(Li-O)_{min}$ from the processes "a" to "c", thus excluding the involvement of A1 and C′ sites in the corresponding reactions. This leaves the A2 site as the candidate responsible for the initial lithiation. Furthermore, only the A2 site shows a gradual increase in geometric size upon early lithiation, as expected due to Li accommodation. For process "d", which, as discussed earlier, appears to be a two-phase reaction, the most prominent change in the Li−O distances is seen for 1/2 $d(O_{br}-O_{br})$ in site C′ which increases by 0.29 Å (about 17%) and the phase that is formed during this process now contains a value for 1/2 $d(O_{br}-O_{br})$ larger than $d(Li-O)_{min}$. This change is also accompanied by an increase in area of site C′, while no volume increase was observed for A1 and A2 sites, suggesting the occupation of the C′ site during the phase transformation. Upon further lithiation, the lengths of the 1/2 $d(O-O)_{diagonal}$ for all the three sites start to lie in the range between $d(Li-O)_{min}$ and $d(Li-O)_{max}$, meeting the criteria to accommodate Li. Particularly for the A1 site, 1/2 $d(O_{3f}-O_{3f})$ is reduced below $d(Li-O)_{max}$ concurrently with a site volume expansion, implying that Li is inserted into this site after the phase transition "d". At higher Li concentrations (>Li 1.0) in process "f", the changes in both 1/2 $d(O-O)_{diagonal}$ and the geometric size of site A1 become less noticeable.

Based on the determined site occupations, we reexamined the PDF refinement more carefully. It is worth noting that the difference patterns from previous PDF refinements (where Li atoms were excluded) for the states beyond Li 0.36 all show a peak above the noise level at about 5.1 Å. This peak becomes particularly prominent in the states with high Li concentrations such as Li 1.27 (see Figure 7a), implying it could be associated with Li-related atom pairs that were previously excluded in all refinements. The pattern at the end of discharge (Li 1.27) was chosen for further study due to its maximum Li content, which in principle should minimize the experimental uncertainty caused by measuring a low Z element using X-rays. To reduce the analytical uncertainty of the refinement and the number of variables that need to be refined we assume full occupation of the three sites (leading to a formula of $Li_{1.25}TiO_2$). The new attempt, based on the previous single-phase refinement, has all variables constrained apart from the scaling factor. Note that we do not mean to infer that $Ti^{2+}$ is formed at this composition (due to a much lower redox potential for the $Ti^{3+}/Ti^{2+}$ reduction);[3] rather much of the additional 0.25 Li is most


DOI: 10.1021/jacs.7b05228
J. Am. Chem. Soc. 2017, 139, 13330−13341

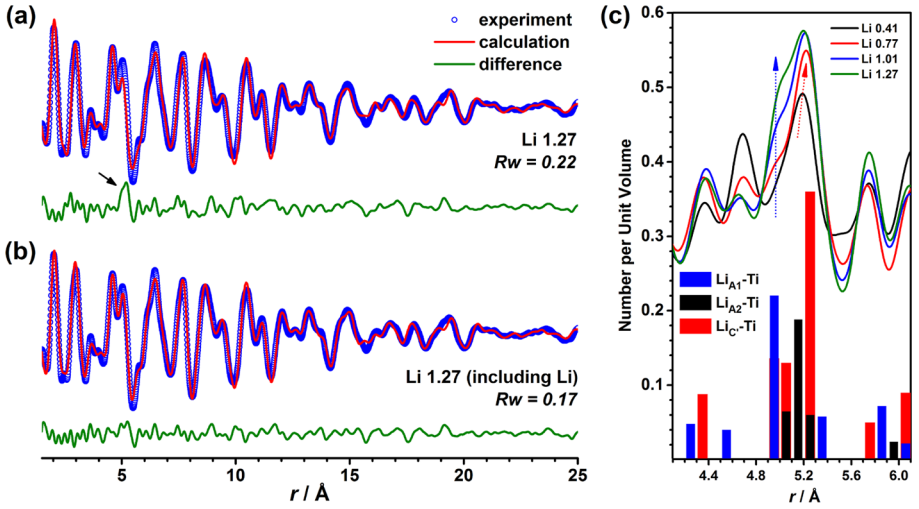


**Figure 7.** Refinement of the PDF for the end of discharge (Li 1.27) (a) excluding and (b) including the Li atoms in the structure. Experiments, calculations, and difference patterns are shown as blue dots and red and green lines, respectively. The black arrow in (a) indicates the major peak above the noise level in the difference pattern. This peak (green) is magnified in (c) and compared with selected difference PDFs from other states of discharge (Li 0.41, 0.77, 1.01, and 1.27). A histogram of atom-pair distances (around 5 Å) between Ti and Li atoms from site A1 (blue), A2 (black), and C′ (red) evaluated from the refined structure for Li 1.01 is also shown below. Red and blue dotted arrows indicate the peak growth and/or shift.

likely associated with surface sites/SEI, the additional Li being consumed via side reactions with hydroxyl surface groups and the electrolyte. This additional Li is, however, difficult to model in these refinements. The Li coordinates, originally taken from theoretical studies (A1 (0.55, 0.00, 0.38),[6] A2 (0.67, 0.00, 0.00),[6] and C′ (0.00, 0.00, 0.00)[3]) were refined. The result showed a significant improvement reflected by a much reduced $R_w$ value from 0.22 to 0.17 and a less noticeable difference peak at 5.1 Å (Figure 7b), with refined Li coordinates of A1 (0.54, 0.00, 0.32), A2 (0.67, 0.00, 0.01), and C′ (0.00, 0.00, 0.00). An examination of the atomic distances using these slightly modified Li positions (Figure S5) shows that no Li−O pairs have distances around 5.1 Å. For Li−Ti and Li−Li pairs, the atomic distances in the third Ti- and Li-coordination shell of Li both have lengths around 5.0 Å. However, the Li−Li pairs are fewer in number and will be weaker due to the lower X-ray scattering factor of Li in comparison to that of Ti; thus, the difference peak at 5.1 Å is dominated by contributions from the Li−Ti pairs. To study this peak more carefully, selected difference patterns (between the calculations performed excluding the Li atoms and the corresponding experiments) are overlaid and compared in Figure 7c. The growth of the peak intensity reflects the increasing number of Li−Ti pairs as a result of higher Li concentrations. A closer study of these peak profiles shows that this peak can be decomposed into two other components, one around 5.2 Å which shows a significant increase from Li = 0.41 to 0.77, accompanied by a small positive shift, and the other around 5.0 Å with growth occurring mainly after the state of Li = 0.77. According to the histogram of the Li−Ti pairs from the three unique Li sites, the component at 5.2 Å agrees well with the main Li−Ti pair distance from site C′ and its growth between state 0.44 and 0.77 is consistent with Li uptake in site C′ in the corresponding process. The component with a shorter distance 5.0 Å matches well the main Li−Ti pair distance from site A1, its growth indicating A1 insertion from state 0.77 onward. The main feature at about 5.1 Å for state 0.44 is consistent with the average Li−Ti distances from site A2. These assignments are in excellent agreement with the aforementioned site occupation deduced from the geometric evolution of the Li sites.

To exploit the X-ray total scattering data fully, we further used the (Bragg) diffraction pattern to validate the proposed Li site occupation at different states. Along with the shape anisotropy of the nanoparticles,[7] Li occupancy will also vary the intensity of some individual reflections leading to a change of the apparent peak profile (see Figure S6). Hence the XRD pattern, although showing severe peak broadening, can still be used to verify the proposed occupation of the Li sites (see SI for more detail). By comparing the XRD peak profile, in terms of relative peak intensities and apparent peak positions, we demonstrate that the simulated patterns incorporating Li atoms with the proposed occupation sequence of A2 > C′ > A1 show excellent agreement with the experiments (Figure S7).

*B. Reaction Mechanism.* The electrochemistry data revealed three steps ("a" to "c") related with A2 site occupation in the initial discharge. In process "a", the load curve (Figure 2a) shows a voltage reduction associated with an initial capacity larger than that observed in the bulk form of $TiO_2$ (B).[17,37] However, there is no prominent feature in the corresponding process in the d$Q$/d$V$ (Figure 3a) and CV (Figures 3b and S2f) plots, suggesting the reaction is probably irrelevant to the $Ti^{3+}$/$Ti^{4+}$ redox couple. A similar voltage drop was also seen in the initial discharge for the nanosized and amorphous anatase phase. This voltage drop was accompanied by an initial capacity that scales with the surface area of the anatase material and was attributed to the reaction of Li with surface adsorbed $H_2O$/−OH species.[38] Considering the $TiO_2$ (B) nanoparticles were prepared in a water-rich environment (using hydrothermal synthesis) and surface −OH species were previously identified by Fourier-transform infrared (FTIR) spectroscopy,[39] we expect a similar surface reaction to that seen for anatase. This reaction forms surface $Li_2O$, which could offer an explanation for the prominent resonance seen around 0 ppm upon early discharge in the $^6$Li NMR results reported previously,[16,38] and which is similar to that found in anatase[38] where such a reaction is rapid and largely irreversible in this


DOI: 10.1021/jacs.7b05228
J. Am. Chem. Soc. 2017, 139, 13330−13341

voltage window. It is, thus, likely a main contribution to the capacity loss observed between the first and subsequent cycles.

The analysis of the rt CV data (Figure 3b) revealed an increasing contribution from a diffusive current (slower process) as the reaction progresses, suggestive of a charge transfer via Li insertion in the bulk. Therefore, Li insertion into the subsurface region (within a couple of Å) of the nanoparticles must be occurring in parallel with the surface reaction. Increasing the temperature results in both more side reactions and more "Faradaic" processes (Figure S2f) (i.e., reduction of subsurface and bulk $Ti^{4+}$). The fact that process "a" is dominated by surface reactions explains the minor changes in the lattice constants during this step.

Upon further lithiation in process "b" and "c", the respective changes in the crystallographic parameters show different evolving trends with the lattice constants in process "c" (particularly lattice constants $a$ and $\beta$) growing more rapidly than those in region "b". These trends indicate that Li incorporation of the A2 site may follow a two-step mechanism resulting in an intermediate phase $Li_{0.25}TiO_2$ in process "b", the A2 site being fully occupied in process "c" leading to $Li_{0.5}TiO_2$. Both reactions show a solid-solution behavior. Subsequent to the A2 site insertion, Li insertion into site C′ takes place in process "d", which is accompanied by a significant volume increase as a result of expansion of the lattice constants $a$, $b$, and $c$. The reaction follows a two-phase mechanism and takes place, particle-by-particle, according to the PDF analysis, leading to a phase transition from $Li_{0.5}TiO_2$ to $Li_{0.75}TiO_2$ where both A2 and C′ sites are fully occupied. However, the PDF analysis does not necessarily distinguish between a two-phase reaction that occurs via a metastable solid solution or one that occurs via a coherent interface.[40]

Further lithiation was found to occur via a solid-solution mechanism, associated with occupancy of the A1 site. Based on the evolution of the lattice constants, this A1 site insertion seems to include two steps. In process "e", a small increase in the unit cell volume and the $b$ lattice parameter is observed while parameters $c$ and $\beta$ show a steady reduction, with the $a$ lattice parameter remaining nearly constant. These changes become less significant in the following process "f"; however, they are still discernible, suggesting further lithiation into site A1 takes place but it is now accompanied by SEI formation. This is consistent with the electrochemistry data collected at higher temperatures (Figures 2 and 3) confirming an increased temperature not only promotes further lithiation of A1 site but also results in concurrent electrolyte decomposition. Such a competing reaction is particularly pronounced in the first discharge, contributing to the capacity loss seen in the subsequent cycles (in addition to the irreversible capacity originating from the surface reaction in the beginning of the discharge, as discussed earlier). Furthermore, the aforementioned intermediate-range structural disorder modeled in our previous morphology study[7] is only discernible in $Li_xTiO_2$ with $x > 0.75$ (Figure S8), indicating the lithiation-induced strain stems from the A1 insertion and is possibly associated with an inhomogeneous distribution of Li in the A1 site.

**Lithiation Kinetics and Li Transport.** We now associate the phase transitions with the electrochemical data to study the lithiation kinetics of the $TiO_2$ (B) nanoparticles. The analysis of the GITT data directly generates information defining Li mobility that is related to the crystal structure and lithiation mechanism. The CV study allows us to correlate the charge storage mechanism with the kinetic behavior derived from the GITT analysis for each redox process; the comparison of the results between 25 and 50 °C further enables us to study the temperature dependence of the charge storage kinetics.

In the prior discussion, we have primarily ascribed the initial lithiation to the Li reaction with the surface-adsorbed −OH groups, a process that shows rapid "capacitive" behavior. As the reaction potential reduces, Li starts to intercalate into the A2 site giving rise to an increasing contribution from a slower process associated with a so-called diffusive (Faradaic) current[5] (Figure 3b) and partly reduced $Ti^{4+}$. This diffusive current eventually becomes comparable to the current attributed to the surface reaction leading to charge storage shared between the capacitive- and diffusion-controlled processes. In addition, the smaller charge on the reduced $Ti^{4+}$ ions may reduce the diffusion barrier, resulting in faster Li transport, consequently an enhanced Li mobility as lithiation progresses. An increased temperature revealed a diffusion-enhanced surface reaction, which is consistent with the increase of $D_{Li}$ in the corresponding process shown in Figure 3a.

Upon further Li incorporation of the A2 site, bulk insertion starts to take place leading to a radical increase in a diffusive contribution seen from the beginning of process "b" to process "c" where a maximum contribution of nearly 100% is reached. However, the corresponding Li mobility in these two processes shows distinct changes: $D_{Li}$ remains high and nearly unchanged in process "b" while a significant reduction of the $D_{Li}$ is observed in process "c". Since these two steps were attributed to the zero-to-half and half-to-full occupation of the A2 site respectively, the observed different Li mobility implies that the mechanisms of these two lithiation steps might be fundamentally different and may involve a change of the Li transport pathway.

For $Li_xTiO_2$ with low Li concentrations ($x < 0.25$), computational studies found that Li migration along the $b$-channel is the most favorable route, involving hops from one C site to another (Figure 8 path I) via C′, and the calculation of energy barriers for Li exchange suggested C → A2 migration (path II) is associated with the lowest energy.[8] Therefore, the initial occupation of the A2 site (process "b") probably follows C → A2 insertion with Li migration along the $b$-channel. For lithiation above $x \geq 0.25$, the occupation of A sites destabilizes site C making C′ more favorable, since the separation between these two sites is only 2.0 Å.[3,9,41] Koudriachova predicted that this site displacement takes place when the A2 site is half full ($Li_{0.25}TiO_2$), which modifies the Li diffusion pathway as well as the A2 site reaction mechanism from C → A2 to C′ → A2 (path III) insertion; moreover, higher diffusion barriers were proposed causing Li to be increasingly trapped in the A2 site when the Li occupancy increased from Li 0.25 to Li 0.5.[9] These predictions from the calculations are in excellent agreement with our observation of an increased diffusive current associated with a noticeably reduced $D_{Li}$ in process "c", indicative of a kinetically much slower process for this second half of the A2 insertion. Regarding Li transport, since the C site is no longer stable after 0.25 Li incorporation, diffusion along the $b$-direction[6,8] (path I) becomes less favorable; in addition, diffusion along the $a$-direction via A2 → A2 migration (path IV) is also improbable due to a high energy barrier involved.[8,41] Consequently, as an alternative, $Li^+$ can either follow a zigzag-like route hopping between C′ and A1 sites along the $b$-channel[41] (path V) or migrate via a path perpendicular to the $b$-axis (along the $c$-axis) via -A1-A1-C′-A1-A1-hops[9] (path VI). Due to the lack of energy references for the barriers associated


DOI: 10.1021/jacs.7b05228
J. Am. Chem. Soc. 2017, 139, 13330−13341

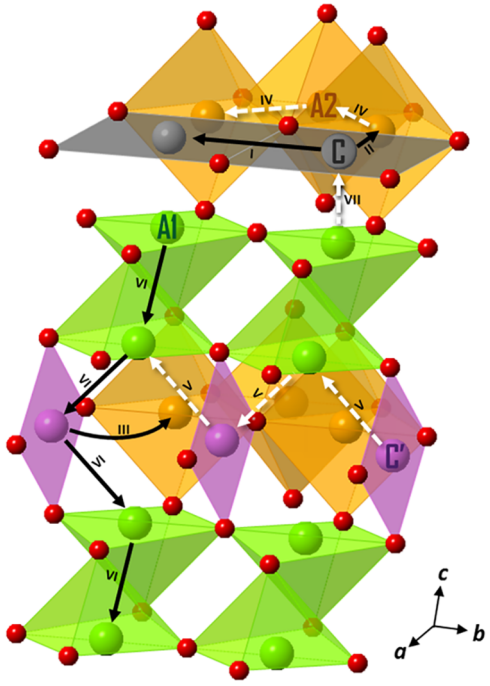


**Figure 8.** Illustration of the probable (black solid arrow) and improbable (white dashed arrow) Li migration pathways marked with roman numerals. The structure shows only the Li sites with $TiO_6$-octahedra omitted for a clearer view.

with A1 → C′ and A1 → A1 migration upon half occupation of the A2 site, it is difficult to conclude which route is more favorable. Nevertheless, at dilute Li concentrations, the barriers for A1 → A1 migration (0.26 eV) are only slightly higher than that of C → C hops (0.22 eV) involved in the straight-line diffusion,[41] and further occupation of the A2 site might render the migration between the neighboring A1 sites more favorable due to the lower Li−Li repulsion between the diffusing $Li^+$ and the Li ions already occupying the A2 site, in comparison with the repulsion experienced in -A1-C′-A1-hops (path V). Hence diffusion along the *b*-channel in the $Li_xTiO_2$ starts to get limited for $x > 0.25$ and migration along the *c*-direction becomes rather competitive. This route in principle should also serve as the pathway for Li transport in the subsequent C′ site insertion (process "d"). Further calculations based on the thermodynamics proposed in this paper are however needed to verify the predicted pathway.

According to the analysis of the kinetics (Figures 3a−b and S2f), the C′ site reaction in process "d" is associated with reduced $D_{Li}$ values in comparison with the values observed in former processes "b" and "c". $D_{Li}$ reaches a local minimum in the middle of the process. Note that the method employed to derive $D_{Li,}$ using Fick's law, is only valid for solid−solution reactions; in the case of a two-phase reaction observed for process "d", the obtained $D_{Li}$ is considered as an apparent value which does not have the same physical meaning as the absolute $D_{Li}$ for single-phase reactions (such as processes "b", "c", and "e")[42] and direct comparison is not necessarily appropriate. Surprisingly, as the discharge reaction proceeds to process "d", it shows an increasing contribution of the nominally fast capacitive process (relative to the so-called diffusion-controlled intercalation step), which is even more prominent under a faster sweep (Figure S9a−b); increasing temperature seems to boost the "diffusion" contribution in process "d", reflected by a slightly reduced capacitive contribution in the 50 °C data. However, from comparison of the capacitive contributions between the processes from "b" to "e" at different temperatures and scan rates (Figure S9a−b), step "d" still appears to be the most rapid bulk insertion process. The GITT data (Figure 2b) are consistent with this conclusion.

In view of the structural change associated with C′ site insertion, apart from the aforementioned volume increase together with a lattice expansion, the increase in the overall Li concentration also leads to a progressive reduction of the Ti oxidation state rendering the $TiO_6$-octahedra more regular. In the nucleation-and-growth reaction model, these crystallographic differences will result in a structural incoherence leading to a phase-boundary-induced strain even if the symmetry remains unchanged in the transition. In the case of the $TiO_2$ (B) nanoparticles, the particle size is on the same order of or smaller than the phase boundary observed in oxides with a two-phase morphology. If this boundary is present, it accounts for a large volume fraction of the primary domain considering the dimension of the nanoparticles is already very small. Since the route without a phase-boundary-induced energy penalty should lead to a lower energy barrier, it is likely that individual $TiO_2$ (B) nanoparticles transform via a metastable solid-solution-like reaction, as proposed for intercalation compounds such as $LiFePO_4$, where the two end-member phases show no change in structural symmetry.[18,30,31] Note that this metastable solid-solution model might be only true for particles with very small sizes (i.e., few nanometers); for nanoparticles with larger domain sizes (such as tens of nanometers), the two-phase reaction "d" could still take place via the domino-cascade model, as the 25 nm anatase nanoparticles, by contrast, appears to react via such a mechanism (particle by particle).[31] Since the analysis of the PDF data to extract the domain sizes of the end member phases, $Li_{0.41}TiO_2$ and $Li_{0.77}TiO_2$, during process "d", showed no change in domain size, consistent with either proposal, it is necessary to perform high-rate scattering measurement for confirmation.

Upon full occupation of the C′ site ($Li_{0.75}TiO_2$), lithiation proceeds with A1 site insertion following a solid-solution route. The reaction is associated with a $D_{Li}$ comparable to that of process "c" (the second half of the A2 site insertion) and an increase in the contribution of a diffusive current relative to process "d" (C′ site insertion). These indicate the reaction kinetics should be similar to process "c" and slower than process "d". Interestingly, the electrochemical features associated with A2 and C′ site filling are present in the d*Q*/d*V* curves (Figure S10) obtained from all morphologies of $TiO_2$ (B) previously studied.[17] They show slightly different peak positions and widths mainly depending on the dimensions of the materials. However, the feature associated with the A1 site was only seen in nanophases such as nanoparticles and nanotubes (with a wall thickness of about 2.5 nm and length of up to several microns parallel with the *b*-axis[37,43,44]) and was absent in the bulk phase (200 nm × 2 μm) and nanowires (35 nm in diameter and 2 μm in length along the *b*-axis, both dimensions closer to that of the bulk phase).[37] This observation indicates the A1 site insertion is kinetically restricted. To understand the origin of this kinetic property, it is necessary to first examine the possible Li transport pathways for A1 site insertion. When the C′ site is fully occupied, the diffusion path along the *c*-direction passing through the original C site (Figure 8 path VII) is still possible. However, full occupation of both


DOI: 10.1021/jacs.7b05228
J. Am. Chem. Soc. 2017, 139, 13330−13341

A2 and C′ sites significantly increases the barrier for A1 → C migration (path VII), due to short C−C′ and C−A2 contacts. An alternative diffusion route follows the same pathway as proposed for A2 (process "c") and C′ insertion but involves additional Li exchange between the C′ and A1 sites. This process may require higher activation energy resulting in a restriction on the reaction kinetics, and consequently an absence of this lithiation step in the bulk form. As indicated by our study of the temperature effect (on the nanoparticles), this insertion process can be promoted at higher temperatures (50 °C), but this is associated with concurrent SEI formation contributing to the observed capacity loss. Therefore, reducing the primary domain size of the material, particularly the dimension along the diffusion direction that restricts intercalation at higher Li contents, seems more practical to tackle this kinetic restriction.

To investigate the kinetic variation between the $TiO_2$ (B) materials with different morphologies, we have examined their geometries in detail. The nanotubes have a circumference along the *a*-direction with the radius of the tubes oriented along the *c*-axis of the $TiO_2$ (B) unit cell.[44] Since the kinetically limiting Li migration path mostly lies along the *c*-direction, the diffusion length for nanotubes is thus similar to the wall thickness and comparable to that of the nanoparticles. This suggests the following: (1) in the nanotubes, $Li^+$ follows a radial diffusion from the surface to the interior, and (2) the nanoparticles and nanotubes should share similar kinetic properties. However, due to the unique morphology of the nanotubes, its internal surface resembles a squeezed *ab*-sheet, while the outer surface contains an expanded lattice.[44] As a result, only part of the material (in the region close to the external surface) retains a good rate performance; in addition, the extreme curvature in the interior may lead to defects rendering certain Li sites less accessible. These explanations could account for the relatively poor capacity at higher cycling rate observed for the nanotubes in comparison with nanoparticles.[17] For nanowires, although they also grow along the *b*-axis with similar dimensions as the nanotubes, they have migration paths parallel to the *ac*-plane with a diffusion length that is 10 times that of the nanotubes. Therefore, the nanowires behave more like the bulk phase rather than nanotubes with a negligible contribution to the capacity from A1 site insertion.

## CONCLUSION

We have performed an *in situ*/*operando* X-ray total scattering experiment to study the change of the local structure of the $TiO_2$ (B) nanoparticles upon lithiation. In addition to the structural study, we also conducted electrochemistry measurements to evaluate Li mobility and charge storage behavior from the GITT and CV data, respectively. Through careful analysis of the evolution of the geometries of the potential sites for Li insertion and careful examination of the difference PDF pattern, further confirmed by a comparison of the simulated and experimental diffraction data, we conclude that Li site occupation follows the sequence A2 > C′ > A1. With the kinetic properties reflected by the electrochemistry results taken into consideration, we found that the actual lithiation mechanism is more complicated than the apparent three-step insertion and is associated with side reactions. The discharge begins with surface reactions involving surface (terminal) −OH groups. These reactions contribute to the capacity loss and are in parallel with Li insertion into the subsurface region of the nanoparticles. The bulk insertion starts with the A2 site via a two-step solid-solution mechanism. Li migration commences down the *b*-direction and involves hopping between the A2 and empty C sites in the larger tunnels. Upon half occupation of A2, repulsion between the Li ions in the A2 sites and the C sites during the diffusion process increases the energy barrier for diffusion; an alternative pathway involving the C′ site is now proposed to play a role in the intercalation process, resulting in Li transport along the *c*-direction. Subsequent C′ site occupation occurs via a two-phase particle-to-particle transformation, which is, of note, a kinetically rapid reaction. The final A1 insertion operates via a solid-solution reaction and is a kinetically restricted step. It is only present in nanostructured phases and can be promoted by raising the operating temperature, which however brings about inevitable SEI formation further leading to a capacity loss. By comparing the fast cycling capabilities of the $TiO_2$ (B) materials between different morphologies, we believe it is important to prepare materials with small dimensions along the diffusion direction that is kinetically limiting at high lithium contents, i.e., the *c*- instead of the *b*-direction, in order to achieve excellent kinetic performance. Further calculations of the migration energy barrier based on the thermodynamic model proposed in this paper will be very important to verify the diffusion pathways and to rationalize the kinetic difference between the various morphologies, providing insight for future material design.

## ASSOCIATED CONTENT

### Supporting Information

The Supporting Information is available free of charge on the ACS Publications website at DOI: 10.1021/jacs.7b05228.

Summary of previously reported computational and experimental studies; Potential curves and the corresponding d*Q*/d*V* from the galvanostatic measurements performed at 25 and 50 °C; CV at 25 and 50 °C with the charge storage analysis for the 0.5 and 5.0 mV/s data; Comparison between the *in situ* and *ex situ* PDFs; Comparison of the single- and two-phase refinements for the *in situ* PDF at Li 0.59; Histogram of Li-containing atom-pair distances; Comparison of XRD simulations including Li atoms between the nanoparticles and bulk phase; d*Q*/d*V* from $TiO_2$ (B) with various morphologies (PDF)

## AUTHOR INFORMATION


### Corresponding Authors

*cpg27@cam.ac.uk
*xiaohua716@gmail.com

### ORCID

Xiao Hua: 0000-0002-8673-5678
Michael G. Fischer: 0000-0002-0519-5463
Karena W. Chapman: 0000-0002-8725-5633
Ullrich Steiner: 0000-0001-5936-339X
Clare P. Grey: 0000-0001-5572-192X


### Notes

The authors declare no competing financial interest.

## ACKNOWLEDGMENTS

We acknowledge the funding from the Swiss NRP70 "Energy Turnaround" program and EPSRC via the "nanoionics" grant. Use of the Advanced Photon Source, an Office of Science User Facility operated for the U.S. Department of Energy (DOE)



DOI: 10.1021/jacs.7b05228
J. Am. Chem. Soc. 2017, 139, 13330−13341

Office of Science by Argonne National Laboratory, was supported by the U.S. DOE under Contract No. DE-AC02-06CH11357. We thank Dr. Kamila M. Wiaderek for the help in the *in situ* PDF experiment. We are also grateful to Dr. Hao Liu, Dr. Ren Yu, Jonathan Lim, Dr. Sylvia Britto, Prof. M. Saiful Islam, and Prof. Martin Dove for many insightful discussions.

## REFERENCES

(1) Schneider, J.; Matsuoka, M.; Takeuchi, M.; Zhang, J.; Horiuchi, Y.; Anpo, M.; Bahnemann, D. W. *Chem. Rev.* **2014**, *114*, 9919−9986.
(2) Wang, Z.-S.; Kawauchi, H.; Kashima, T.; Arakawa, H. *Coord. Chem. Rev.* **2004**, *248*, 1381−1389.
(3) Dalton, A. S.; Belak, A. A.; Van der Ven, A. *Chem. Mater.* **2012**, *24*, 1568−1574.
(4) Dylla, A. G.; Henkelman, G.; Stevenson, K. J. *Acc. Chem. Res.* **2013**, *46*, 1104−1112.
(5) Wang, J.; Polleux, J.; Lim, J.; Dunn, B. *J. Phys. Chem. C* **2007**, *111*, 14925−14931.
(6) Arrouvel, C.; Parker, S. C.; Islam, M. S. *Chem. Mater.* **2009**, *21*, 4778−4783.
(7) Hua, X.; Liu, Z.; Bruce, P. G.; Grey, C. P. *J. Am. Chem. Soc.* **2015**, *137*, 13612−13623.
(8) Panduwinata, D.; Gale, J. D. *J. Mater. Chem.* **2009**, *19*, 3931−3940.
(9) Koudriachova, M. V. *Surf. Interface Anal.* **2010**, *42*, 1330−1332.
(10) Morgan, B. J.; Madden, P. A. *Phys. Rev. B: Condens. Matter Mater. Phys.* **2012**, *86*, 035147.
(11) Dylla, A. G.; Xiao, P.; Henkelman, G.; Stevenson, K. J. *J. Phys. Chem. Lett.* **2012**, *3*, 2015−2019.
(12) Ishii, Y.; Okamura, K.; Matsushita, T.; Kawasaki, S. *Mater. Express* **2012**, *2*, 23−36.
(13) Armstrong, A. R.; Arrouvel, C.; Gentili, V.; Parker, S. C.; Islam, M. S.; Bruce, P. G. *Chem. Mater.* **2010**, *22*, 6426−6432.
(14) Okumura, T.; Fukutsuka, T.; Yanagihara, A.; Orikasa, Y.; Arai, H.; Ogumi, Z.; Uchimoto, Y. *J. Mater. Chem.* **2011**, *21*, 15369−15377.
(15) Fehse, M.; Ben Yahia, M.; Monconduit, L.; Lemoigno, F.; Doublet, M.-L.; Fischer, F.; Tessier, C.; Stievano, L. *J. Phys. Chem. C* **2014**, *118*, 27210−27218.
(16) Hoshina, K.; Harada, Y.; Inagaki, H.; Takami, N. *J. Electrochem. Soc.* **2014**, *161*, A348−A354.
(17) Ren, Y.; Liu, Z.; Pourpoint, F.; Armstrong, A. R.; Grey, C. P.; Bruce, P. G. *Angew. Chem., Int. Ed.* **2012**, *51*, 2164−2167.
(18) Wagemaker, M.; Borghols, W. J. H.; Mulder, F. M. *J. Am. Chem. Soc.* **2007**, *129*, 4323−4327.
(19) Wen, C. J.; Boukamp, B. A.; Huggins, R. A.; Weppner, W. *J. Electrochem. Soc.* **1979**, *126*, 2258−2266.
(20) Borkiewicz, O. J.; Shyam, B.; Wiaderek, K. M.; Kurtz, C.; Chupas, P. J.; Chapman, K. W. *J. Appl. Crystallogr.* **2012**, *45*, 1261−1269.
(21) Hua, X.; Robert, R.; Du, L.-S.; Wiaderek, K. M.; Leskes, M.; Chapman, K. W.; Chupas, P. J.; Grey, C. P. *J. Phys. Chem. C* **2014**, *118*, 15169−15184.
(22) Hammersley, A., 1998, *FIT2D V9.129 reference manual V3.1. ESRF internal report 98HA01T. ESRF*.
(23) Qiu, X.; Thompson, J. W.; Billinge, S. L. J. *J. Appl. Crystallogr.* **2004**, *37*, 678.
(24) Chapman, K. W.; Chupas, P. J.; Halder, G. J.; Hriljac, J. A.; Kurtz, C.; Greve, B. K.; Ruschman, C. J.; Wilkinson, A. P. *J. Appl. Crystallogr.* **2010**, *43*, 297−307.
(25) Farrow, C. L.; Juhas, P.; Liu, J. W.; Bryndin, D.; Božin, E. S.; Bloch, J.; Proffen, T.; Billinge, S. J. L. *J. Phys.: Condens. Matter* **2007**, *19*, 335219.
(26) Proffen, T.; Neder, R. B. *J. Appl. Crystallogr.* **1999**, *32*, 838−839.
(27) Lindström, H.; Södergren, S.; Solbrand, A.; Rensmo, H.; Hjelm, J.; Hagfeldt, A.; Lindquist, S.-E. *J. Phys. Chem. B* **1997**, *101*, 7717−7722.
(28) Feist, T. P.; Davies, P. K. *J. Solid State Chem.* **1992**, *101*, 275−295.
(29) Egami, T.; Billinge, S. J. L. *Underneath the Bragg Peaks Structural Analysis of Complex Materials*; Pergamon: Kidlington, Oxford, 2012.
(30) Liu, H.; Strobridge, F. C.; Borkiewicz, O. J.; Wiaderek, K. M.; Chapman, K. W.; Chupas, P. J.; Grey, C. P. *Science* **2014**, *344*, 1252817.
(31) Liu, H.; Grey, C. P. *J. Mater. Chem. A* **2016**, *4*, 6433−6446.
(32) Shannon, R. *Acta Crystallogr., Sect. A: Cryst. Phys., Diffr., Theor. Gen. Crystallogr.* **1976**, *32*, 751−767.
(33) Perez-Flores, J. C.; Garcia-Alvarado, F.; Hoelzel, M.; Sobrados, I.; Sanz, J.; Kuhn, A. *Dalton Trans.* **2012**, *41*, 14633−14642.
(34) Deschanvres, A.; Raveau, B.; Sekkal, Z. *Mater. Res. Bull.* **1971**, *6*, 699−704.
(35) Koudriachova, M. V.; de Leeuw, S. W.; Harrison, N. M. *Phys. Rev. B: Condens. Matter Mater. Phys.* **2004**, *69*, 054106.
(36) Kataoka, K.; Takahashi, Y.; Kijima, N.; Nagai, H.; Akimoto, J.; Idemoto, Y.; Ohshima, K.-i. *Mater. Res. Bull.* **2009**, *44*, 168−172.
(37) Liu, Z.; Andreev, Y. G.; Robert Armstrong, A.; Brutti, S.; Ren, Y.; Bruce, P. G. *Prog. Nat. Sci.* **2013**, *23*, 235−244.
(38) Borghols, W. J. H.; Lützenkirchen-Hecht, D.; Haake, U.; Chan, W.; Lafont, U.; Kelder, E. M.; van Eck, E. R. H.; Kentgens, A. P. M.; Mulder, F. M.; Wagemaker, M. *J. Electrochem. Soc.* **2010**, *157*, A582−A588.
(39) Andreev, Y. G.; Panchmatia, P. M.; Liu, Z.; Parker, S. C.; Islam, M. S.; Bruce, P. G. *J. Am. Chem. Soc.* **2014**, *136*, 6306−6312.
(40) Strobridge, F. C.; Liu, H.; Leskes, M.; Borkiewicz, O. J.; Wiaderek, K. M.; Chupas, P. J.; Chapman, K. W.; Grey, C. P. *Chem. Mater.* **2016**, *28*, 3676−3690.
(41) Zhang, Q.; Kaghazchi, P. *J. Phys. Chem. C* **2016**, *120*, 22163−22168.
(42) Zhu, Y.; Wang, C. *J. Phys. Chem. C* **2010**, *114*, 2830−2841.
(43) Armstrong, G.; Armstrong, A. R.; Canales, J.; Bruce, P. G. *Chem. Commun.* **2005**, 2454−2456.
(44) Andreev, Y. G.; Bruce, P. G. *J. Am. Chem. Soc.* **2008**, *130*, 9931−9934.



DOI: 10.1021/jacs.7b05228
*J. Am. Chem. Soc.* 2017, 139, 13330−13341